ORIGINAL ARTICLE

Microstructural evolution and mechanical properties of a low-carbon low-alloy steel produced by wire arc additive manufacturing

Mehran Rafieazad[1] (ID) · Mahya Ghaffari[1] · Alireza Vahedi Nemani[1] · Ali Nasiri[1]

Abstract

The emerging technology of wire arc additive manufacturing (WAAM) has been enthusiastically embraced in recent years mainly by the welding community to fabricate various grades of structural materials. In this study, ER70S-6 low-carbon low-alloy steel wall was manufactured by WAAM method, utilizing a gas metal arc welding (GMAW) torch translated by a six-axis robotic arm, and employing advanced surface tension transfer (STT) mode. The dominant microstructure of the fabricated part contained randomly oriented fine polygonal ferrite and a low-volume fraction of lamellar pearlite as the primary micro-constituents. Additionally, a small content of bainite and acicular ferrite were also detected along the melt-pool boundaries, where the material undergoes a faster cooling rate during solidification in comparison with the center of the melt pool. Mechanical properties of the part, studied at different orientations relative to the building direction, revealed a comparable tensile strength along the deposition (horizontal) direction and the building (vertical) direction of the fabricated part (~400 MPa and ~500 MPa for the yield and ultimate tensile strengths, respectively). However, the obtained plastic tensile strain at failure along the horizontal direction was nearly three times higher than that of the vertical direction, implying some extent of anisotropy in ductility. The reduced ductility of the part along the building direction was associated with the higher density of the interpass regions and the melt-pool boundaries in the vertical direction, containing heat-affected zones with coarser grain structure, brittle martensite–austenite constituent, and possibly a higher density of discontinuities.

Keywords Additive manufacturing (AM) · Wire arc additive manufacturing (WAAM) · Low-carbon low-alloy steel · Microstructure · Mechanical properties

1 Introduction

Additive manufacturing (AM) is a novel manufacturing technology in which a component is fabricated by depositing the feedstock material layer-by-layer to build a fully functional, dense, and 3D-shaped component [1–3]. A wide range of different metals, composites, and polymers can be used as the feedstock material employing various AM techniques.

The additive manufacturing of metallic components can be classified based on the adopted feedstock materials into three main categories, i.e., powder-bed processes, such as selective laser melting (SLM) or direct metal laser sintering (DMLS), powder feed processes, such as laser metal deposition (LMD), also known as direct laser fabrication (DLF), and wire-feed processes, such as wire arc additive manufacturing (WAAM) [4, 5]. WAAM is an AM technology that usually benefits from a robotic arm, carrying an arc welding torch as the energy source to fabricate metallic parts additively in the form of weld beads overlaid on previously deposited layers [6, 7]. In WAAM, all the consumable wire is continuously fed into the adopted electric arc or plasma and entirely melted [8, 9], leading to extremely high deposition rates associated with this process (3–8 kg/h), which is drastically higher than that in the powder-bed/feed AM systems (0.1–0.6 kg/h) [4]. Therefore, it is mostly suited for fabrication of large-scale engineering components with more simple geometries and less complexity in design [9–11].

The most commonly used welding processes integrated with the WAAM technology are gas tungsten arc (GTA) and gas metal arc (GMA) welding processes [12]. In recent years, in multiple studies [12–14], the capabilities of the GMAW-

✉ Mehran Rafieazad
mrafieazad@mun.ca

[1] Faculty of Engineering and Applied Science, Memorial University of Newfoundland, St. John's, NL A1B 3X5, Canada

based WAAM in terms of technological issues and metallurgical properties for different alloys have been widely explored. For instance, the microstructure and tensile properties of 316 L austenitic stainless steel fabricated by GMA-AM [12], the feasibility of depositing steel parts by means of double electrode GMAW-based AM system [14], and the effect of the main deposition process parameters on the surface roughness of low-carbon steel parts fabricated using GMAW-based additive manufacturing [13] have been investigated.

From the fabrication perspective, there are many similarities between conventional GMAW and wire arc additive manufacturing methods, leading to analogous challenges and difficulties associated with both processes. For instance, the strength–ductility combinations in steels can be affected adversely from the thermal cycles experienced during layer-by-layer deposition of WAAM, correlated to either the heat-affected zone (HAZ) softening [15–17] and/or formation of localized brittle zones (LBZs) along the interpass regions, commonly observed in the multi-pass welding processes [18, 19]. Therefore, adopting an arc welding process with a low-heat input-transfer mode seems to be favorable for the purpose of WAAM.

Another complexity associated with the WAAM of ferrous alloys is that depending on the carbon content, alloying elements, and cooling rate of the steel, the manufactured component in the as-printed condition may possess a blend of different microstructures, e.g., ferrite, Widmanstätten ferrite, bainite, martensite, or acicular ferrite [20]. Thus, to obtain a desired microstructure with adequate strength and toughness in a WAAM part, the GMAW process essential parameters should be carefully selected [21].

In a recent study, Liberini et al. [1] characterized the microstructure of a wall-shape product obtained by the successive deposition of weld beads using an ER70S-6 steel wire through GMA-AM. The authors reported microstructural inhomogeneity across the deposited wall in the sequence of a bainitic lamellar structure at the upper zone of the wall, equiaxed grains of ferrite in the middle, and a ferritic structure with thin strips of pearlite at the lower zone [1]. Consequently, it was concluded that different thermal cycles associated with the layer-by-layer deposition nature of the WAAM can result in various microstructures from the top to the bottom of the manufactured walls [1]. While the mechanical properties of the fabricated walls were not reported in their study [1], such microstructural non-uniformity across the building direction could lead to anisotropic mechanical properties.

It is reported in multiple studies [22–25] that the high cooling rate and temperature gradient experienced throughout the components during the AM fabrication process dictate the grain growth direction and morphology, yielding heterogeneous microstructures and anisotropic mechanical properties. However, lower thermal input WAAM-based processes, such as WAAM–cold metal transfer (CMT) technique, can result in

a more uniform microstructure and homogenous hardness profile [26]. Wang et al. [27] also showed that in a 304-L austenitic stainless steel wall produced by directed energy deposition additive manufacturing, applying lower heat inputs resulted in a finer microstructure, and, therefore, higher yield and tensile strengths than those in the wall fabricated using a higher heat input. They also reported that at a specific heat input, the coarser microstructure at the top of the walls compared with the bottom of the components resulted in a lower yield and tensile strengths due to a lower cooling rate at the top areas of the wall [27].

Wilson-Heid et al. [22] studied the relationship between the microstructure and the anisotropy in ductility of an additively fabricated Ti-6Al-4V and concluded that the elongation percentage in the transverse direction is higher than that of the longitudinal direction. Wang et al. [28] also reported the anisotropic mechanical properties in a WAAM Ti-6Al-4V alloy, showing a higher strength and lower ductility in the horizontal direction compared with the building (vertical) direction. The authors correlated such properties to the existence of different crystallographic textures along the deposition direction versus the building direction developed from the directional columnar growth of Ti grains during solidification. On the other hand, Haden et al. [29] observed no obvious anisotropy in mechanical properties such as yield and tensile strength in a low-carbon low-alloy steel (ER70S-6) produced via WAAM. However, in their study, the reported mechanical properties were not clearly correlated to the microstructure of the additively manufactured wall. In a recent study by Sridharan et al. [20], a GTA welding system was used to additively manufacture the low-carbon low-alloy steel ER70S-6 along the X-, Y-, and Z-directions followed by a detailed mechanical properties investigation. A significant scatter in the elongation with respect to the sample directions was reported and correlated to the differences in the level of porosities and discontinuities and the localized variations of the microstructural features in each sample.

In addition to all the experimental research on the advancement of the WAAM technology and its accelerated adoption in manufacturing of various engineering materials, the simulation and modeling of various aspects of the process have been also the focus of several studies. For example, the thermal history of the process [30], the deposition path [4, 11], and the dynamics of metal transfer [31] during the fabrication process have been modeled in previous studies. In a study by Fachinotti et al. [30], a thermal-microstructural model capable of describing the thermal history of the WAAM process during the fabrication of Ti-6Al-4V alloy wall was developed. The proposed model was also capable of predicting important microstructural features in the fabricated part based on the predicted thermal history of the process [30]. In another study, the metal transfer dynamics of a wire feeding-based 3D printing process was extensively investigated, and a correlation model between the

process parameters, such as heat input and scanning strategy, and the deposited bead geometry was developed [31].

It is well established that high-heat input-welding processes can lead to coarsening of the ferrite grains in steels due to recrystallization or abnormal phase transformation from Austenite [32, 33]. The result can be a significant HAZ softening and a noticeable reduction in HAZ toughness. This issue is even more critical in the WAAM process due to the multi-pass nature of the process. Therefore, adopting a fast cooling version of the GMAW/GTAW process would plausibly favor the HAZ toughness of the WAAM-fabricated steels.

Surface tension transfer (STT) is an advanced current-controlled short-circuit metal transfer mode in the GMAW process developed by the Lincoln Electric Company [34]. The unique feature of the STT transfer mode is that it offers a combined reduction in energy and improved energy control through droplet by droplet control of the fusion zone, which can be beneficial in minimizing the extent of HAZ softening and can achieve a smooth bead profile and improved bead geometry [34, 35]. The heat input associated with the STT-GMAW process can be as low as 20% of that in conventional spray or pulsed-GMAW processes [34]. Hence, a fast cooling process, such as STT-GMAW, can dramatically enhance the HAZ toughness of high-strength low-alloy steels. The capabilities of this particular transfer mode for the WAAM of metallic components are hitherto unreported.

In the context of WAAM, a large number of studies to date have been carried out on the fabrication of Ti-6Al-4V, but not so much on steels, which are the most commonly used materials in modern industry with an unlimited number of applications in various industrial sectors [29, 31]. Therefore, this study aims at fabricating a low-carbon low-alloy steel (ER70S-6) using wire arc additive manufacturing technique. For the first time herein, the surface tension transfer (STT) waveform control technology was adopted in wire arc additive manufacturing of the part. The used feedstock wire is commonly utilized for the welding of high-strength low-alloy steels owning moderate amounts of scale or rust with widespread applications including structural steels, auto bodies, pipes, fittings, castings, and forgings [36]. This article presents a detailed study of the microstructure and mechanical properties of the WAAM thin-wall parts. Additionally, the influence of the manufacturing process on the anisotropy of the mechanical properties was investigated, utilizing tensile testing and fractography techniques along both vertical and horizontal directions.

2 Experimental Procedure

### 2.1 Materials and fabrication process

The used robotic WAAM platform, the fabricated wall, and its graphical representation are shown in Fig. 1. Each deposited layer on the x-y plane was comprised of six beads with a length of 135 mm and the total height of about 150 mm, containing 50 consecutive layers. The layers have a 3-mm center-to-center overlap, leading to the total width of 22 mm for the wall and the resulting beads for each layer have a height of around 3 mm. The base plate was ASTM A36 mild steel with 12 mm thickness, which was thoroughly cleaned using stainless steel wire brushing and degreased by acetone prior to the WAAM to avoid porosity formation during the fabrication process. As drawn in Fig. 1b, a y-scanning strategy with alternating directions, and 3 mm overlap along the x-axis between the successive passes on each x-y layer was used (y-axis is aligned with the longer dimension of the base plate). The adopted alternating direction scanning strategy was found to contribute to the uniformity of the deposited beads' profile at both ends of the y-axis, resulted in fabricating a straight wall. Moreover, the presented patterns on the front face (y-z plane) of the schematic in Fig. 1b show the locations where vertical and horizontal tensile test samples were machined from the fabricated wall. Also, the squares labeled as the top, middle top, middle bottom, and the bottom on the front face show the location of the samples that were subjected to the microstructure and phase characterization analysis. Figure 1 c is the side overview of the fabricated wall herein.

The ER70S-6 wire with 0.889 mm (0.035 in.) diameter was used as the feedstock material with the chemical composition given in Table 1. A Lincoln Electric GMAW machine with a torch mounted on a 6-axis Fanuc robot was employed as the power source of the process (Fig. 1a). The process was carried out using the following parameters: an arc current of 320 A, an arc voltage of 28 V, a wire feeding rate of 104 mm/s (245 in./min), a scan rate of 5 mm/s (12 in./min), and pure argon as the shielding gas with the flow rate of 45 L/min. Additionally, advanced STT current-controlled short-circuit transfer process was used herein to minimize the heat input of the process and reduce the surface irregularities, the generated fume, and spattering during the fabrication process. To further minimize the effects of consecutive thermal cycles on the microstructure of the previously deposited layers, a 10-min interlayer dwell time was implemented in the fabrication program after the completion of each x-y layer. The selected time interval allowed each layer to be cooled to a temperature below 165 °C (325 °F) [37] before each new layer was deposited. Consequently, a steady-state deposition and a more homogenous microstructure in all layers of the wall along the building direction would be expected due to the similarity of the thermal cycle associated with the solidification of each layer.

Following the fabrication process, the base plate was cut off and separated from the fabricated portion prior to the microstructure and mechanical properties characterization to eliminate any effect resulted from the dilution at the bottom side of the component.

Fig. 1 **a** The used robotic
WAAM platform. **b** Schematic
illustration of the WAAM-
ER70S-6 steel wall. **c** The
manufactured wall using WAAM
method
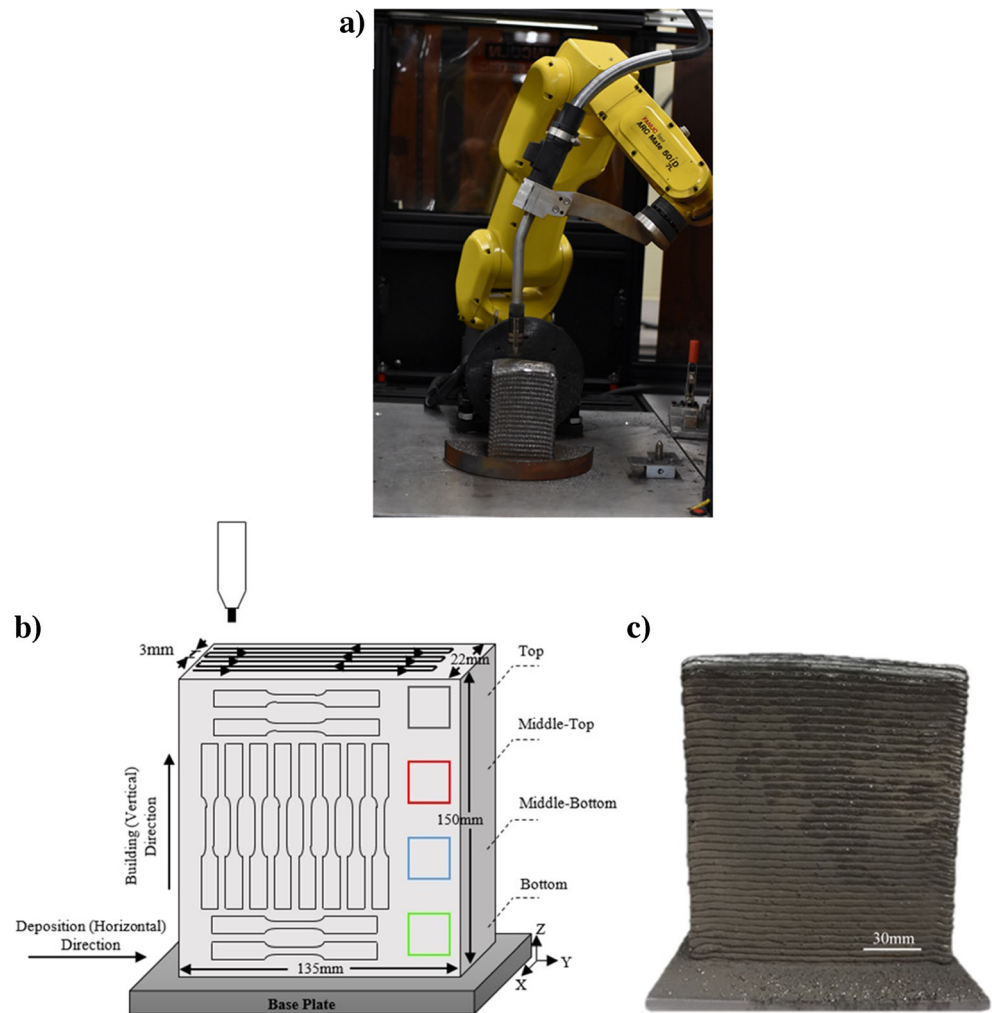
2.2 Microstructure characterization

To perform microstructural characterization and investigate
possible microstructural anisotropy in the printed wall, four
samples from different locations of the wall, including the
bottom, middle bottom, middle top, and the top were sec-
tioned along both the deposition direction and the building
direction (illustrated in Fig. 1b). Standard steel grinding and
polishing procedures were applied utilizing a Tegramin-30
Struers auto-grinder/polisher followed by etching using 5%
Nital as the reagent. The microstructure of all specimens was
examined using an optical microscope (Nikon Eclipse 50i)
and a field emission scanning electron microscope (FEI
MLA 650F). Phase characterization was carried out by means
of a Rigaku Ultimate IV X-ray diffraction (XRD) with Cu-K$_\alpha$

source at 40 kV and 44 mA at the diffraction angle range of
5°–90° with a step size of 0.02°. Electron backscatter diffrac-
tion (EBSD) analysis was also conducted over an area of
$600 \times 600~\mu m^2$ on polished samples with a step size of
1.4 μm and a tilt angle of 70°, using Nordlys II HKL EBSD
detector, Oxford Instruments. To post-process the obtained
EBSD data, the HKL Inc. software, known as Channel 5,
was employed.

2.3 Mechanical properties measurement

Vickers microhardness testing was conducted on different
areas of the wall including the bottom, middle bottom, middle
top, and the top (see Fig. 1a), utilizing a Buehler Micromet
hardness test machine at a load of 3 N and the loading time of

Table 1 The nominal chemical composition of the ER70S-6 feedstock wire (wt%)

C	Mn	Si	Cr	Ni	Mo	S	V	Cu	P	Fe
0.06–0.15	1.40–1.85	0.80–1.15	0.15 max	0.15 max	0.15 max	0.04 max	0.03 max	0.50 max	0.03 max	Bal.

45 s. It should be noted that the reported microhardness test results for each sample in this study are the average value of 5 different indentation points on polished surfaces. The tensile test samples were prepared based on the ASTM E8m-04 standard subsize specimen [38] with 5 mm thickness, 25 mm gauge length, and 100 mm total length. Tensile properties were measured using an Instron load frame with a crosshead speed of 8 mm/min. It is also notable that the strain data was recorded using an extensometer. The horizontal specimens were machined from both the top and bottom zones of the wall, and the vertical tensile specimens were selected from the middle part of the wall, shown schematically in Fig. 1b. In order to avoid the effect of endings, where the scanning direction is reversed and the arc experiences some degree of unstability, and also to eliminate the dilution effect of the base plate, the microstructural characterization and mechanical testing herein were only conducted on an effective area 15 mm away from both ends and 10 mm above the base plate. Repeatability of the results was measured by testing at least five samples under the same conditions to obtain a reliable average value. The fractured surfaces of the tensile test samples from both vertical and horizontal directions were also studied using the SEM. For each direction, three fractured

samples were analyzed to ensure the consistency of the reported features between the samples from the same direction.

3 Results and discussion

3.1 Microstructure characterization

Figure 2 a demonstrates the overall microstructure of the ER70S-6 steel wall at different regions, showing the variation of the microstructure from an area in the vicinity of a fusion line towards the center of the melt pool (top left corner of the image). Figure 2 b and d depict the dominant microstructure of each melt-pool center composed of the typical fine polygonal ferrite (F) as the primary phase and a low-volume fraction of the lamellar pearlite (P) phase, which has primarily formed along the ferrite grain boundaries. Similar microstructural features were reported in a previous study for a WAAM-fabricated ER70S-6 wall [29]. In addition, a closer look at the microstructure along the melt-pool boundaries (Fig. 2c, e) confirmed the formation of acicular ferrite along with bainite regions (AF + B) adjacent to the melt-pool boundary. This transition in microstructure is developed because of the

Fig. 2 Optical micrographs taken from **a** the WAAM-ER70S-6 steel wall at the fusion line and center of the melt pool. **b** Higher magnification of the enclosed area in **a** shown by B, and the inserted image shows an example of a phase fraction analysis micrograph, presenting the distribution of the pearlite phase (in red) along the ferrite grain boundaries. **c** The enclosed area in **a** shown by C. *SEM* micrographs from **d** the enclosed area in **b** shown by D. **e** The enclosed area in **c** shown by E
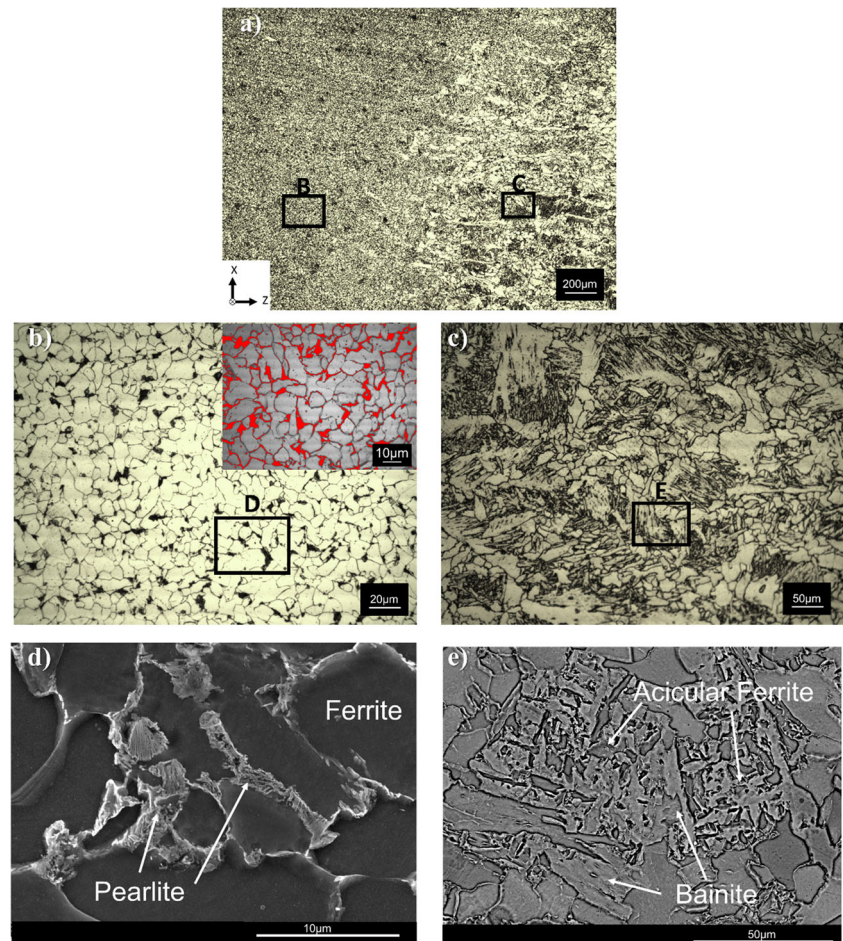
overlapping scanning lines and solidification of individual melt pools, resulting in different thermal histories from the center of each melt pool to the boundaries of its adjacent melt pools [39]. Since the fusion boundaries experience a higher cooling rate during solidification process compared with the center of the melt pools, the formation of some non-equilibrium AF + B phases was detected adjacent to the fusion lines. In a past study, Haselhuhn et al. [40] analogously reported the transition of polygonal ferrite to acicular ferrite from the melt-pool center to the melt-pool boundary in a WAAM-ER70S-6 wall due to faster cooling rates that the material experiences during solidification along the fusion line.

To quantify the volume fraction of the pearlite phase formed along the ferrite grain boundaries, a detailed image analysis of the microstructure taken from various locations of the sample was performed using the ImageJ software (an example is shown in the inserted image in Fig. 2b, in which the red phase corresponds to the pearlite). Due to the low-carbon content of the feedstock wire (0.06–0.15%), the volume fraction of the pearlite phase was approximated to be only $12.54 \pm 0.56\%$ of the total microstructure (the red highlighted phase shown in Fig. 2b).

As compared with the ferrite and pearlite phases, the volume fraction of the acicular ferrite and bainite phases that formed predominantly along the fusion boundaries were negligible (as evident from the micrographs in Fig. 2). The presence of a small volume fraction of bainite and acicular ferrite has been also reported in the microstructure of API-X70 pipeline steel, which is commonly being welded using ER70S-6 filler wire [41]. In particular, bainite offers a higher strength and toughness due to its smaller grain size and higher dislocation density as a result of providing obstacles to dislocation movement as compared with the polygonal ferrite [41]. In the context of the microstructural modifications of the as-printed additively manufactured components, implementing a post-printing heat treatment would be an alternative to modify and refine the microstructure and ultimately improve the mechanical performance of the printed sample, which is the subject of a future study by the authors.

It should be noted that the aforementioned microstructural features were observed throughout all layers of the component from the bottom to the top zones of the wall. Therefore, a uniform microstructure could be obtained in different zones of the WAAM-manufactured part, albeit some degree of inhomogeneity was detected in each deposited bead from the melt-pool center towards its boundary. Such uniformity in the microstructure along the building direction of the wall could be attributed to the sequence of the layer deposition and the adopted interlayer dwell period. It is well established that in metal additive manufacturing processes, the existence of multiple and complex thermal cycles is the primary factor leading to the non-uniformity of microstructure along the building direction [20, 42]. However, as stated in the experimental

procedure section, a 10-min interval between each layer can minimize the effect of heat accumulation and avoid microstructural variations in different layers across the z-direction. Therefore, all layers have experienced approximately consistent heating and cooling cycles, resulting in a uniform microstructure along the building direction.

As a complement to the SEM analysis, an EBSD analysis was performed to obtain more information on crystallographic texture and orientation features of the printed sample. The EBSD inverse pole figure (IPF-z) map of the as-printed sample along the building direction (z-axis) is demonstrated in Fig. 3a. The IPF-z map illustrates comprehensive information on the grains' orientation/misorientation, their size, and aspect ratio. To quantify the detailed information of the grains, the IPF maps were evaluated through statistical analysis of the grain area, misorientation angle, and grains' aspect ratio, shown in Fig. 3 b, c, and d, respectively.

The IPF map and the statistical distribution of the grain area and the aspect ratio show that the wall is mainly composed of randomly oriented equiaxed grains (aspect ratio < 3) with an average grain size of ∼ 7.30 μm. The grain size is considered one of the most prominent microstructural characteristics that affects the mechanical properties. The grain coarsening in the HAZ of the previously deposited track is clearly visible in the IPF map, denoted by the coarse grain region with an average grain size of 15.76 ± 2.34 μm, whereas the area inside the melt pool revealed a noticeably smaller grain size (4.94 ± 1.26 μm). Considering the nature of layer-by-layer deposition associated with the WAAM method, each deposited layer reheats the previous one. The resulting high temperature in the previously solidified track would facilitate the grain boundaries migration and consequently causes grain growth in the vicinity of each melt-pool boundary. Such microstructural inhomogeneities in the structure of the printed component can adversely impact the mechanical properties of the part and contribute to anisotropic mechanical properties. As depicted in the grain area distribution plot (Fig. 3b), the majority of the grains (approximately 80%) have an area smaller than 100 μm², representing an overall fine grain structure for the as-printed WAAM-ER70S-6 part. The misorientation distribution graph (Fig. 3c) confirms that the misorientation angle of the grains is mostly distributed between 0 and 4 degree, corresponding to a uniform orientation of the cubic structure [43].

The statistical distribution of the grain shape aspect ratio is plotted in Fig. 3d. The grain shape aspect ratio can be used as a criterion to differentiate the equiaxed grains from the columnar grains. A grain would be considered an equiaxed grain when its shape aspect ratio is smaller than 3, whereas columnar grains possess aspect ratios of ≥ 3 [44, 45]. As revealed by the grains' aspect ratio distribution graph (Fig. 3d), more than 90% of the grains possess an equiaxed shape and only a small portion of the grains (<6%) were characterized by a columnar shape.
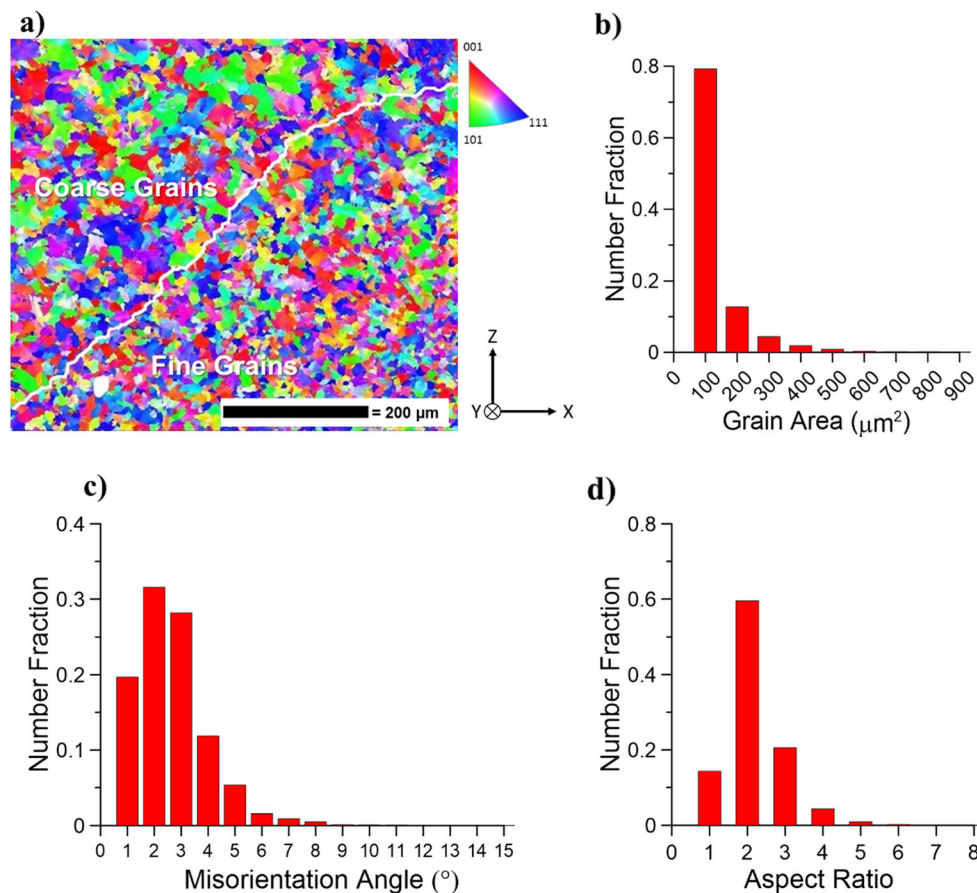
Fig. 3 **a** EBSD inverse pole figure map of the as-printed WAAM-ER70S-6 sample. Statistical distribution plots showing the distribution of **b** grain area, **c** misorientation angle, and **d** grain shape aspect ratio

The pole figures (PFs) from the EBSD map shown in Fig. 3a were determined to investigate the texture distribution produced by the manufacturing process of the sample, and the result is demonstrated in Fig. 4. The {100}, {110}, and {111} pole figures of the WAAM-ER70S-6 sample are illustrated in Fig. 4. The X and Y directions are shown on the {100} pole figure, and the Z-axis is normal to the plane of the pole figure. The PF maps revealed a weak texture, representing a random texture with a maximum intensity of 3.08 above the random background.

The XRD analysis of the WAAM-ER70S-6 wall was conducted for phase identification on the samples extracted from different heights along the building direction (shown in Fig. 1b), and the obtained spectras are presented in Fig. 5. As clearly revealed, the as-printed wall predominantly contains an α-Iron (BCC, Ferrite) phase as the main constituent, in which the α-Iron peaks are located at 2θ of approximately 44.55°, 64.85°, and 82.11° according to the JCPDS patterns of 98-000-9982. The XRD measurements also revealed the absence of an austenite (Iron-FCC) phase, confirming that either the retained austenite has not formed in the as-printed sample or its volume fraction is too low, below the detection limit of the XRD. The precipitated cementite phase (in the

form of lamellae in the pearlite phase) was also not detected on the XRD spectra due to its drastically lower volume fraction as compared with the ferrite phase. The identical XRD patterns obtained from different locations across the building direction (shown in Fig. 5) is another compelling piece of evidence for the uniformity and homogeneity of the microstructure along the building direction of the wall.

3.2 Mechanical properties

Figure 6 presents the overall Vickers microhardness variation of the as-printed component along the building (vertical) direction from the bottom to the top of the wall with 10 mm margin from the bottom and top of the wall to eliminate the effects of both dilution and the last deposited layer. The microhardness testing results (Fig. 6a) revealed that the overall average microhardness of the sample was 160 ± 7 HV throughout the whole sample, indicating a uniform hardness distribution across the building direction due to the consistency of the microstructure along the building direction. A uniform microhardness profile is generally favored as it represents more homogeneous and isotropic micro-mechanical properties in the fabricated part [20]. The evenly distributed

Fig. 4 Pole figures from the WAAM-ER70S-6 wall
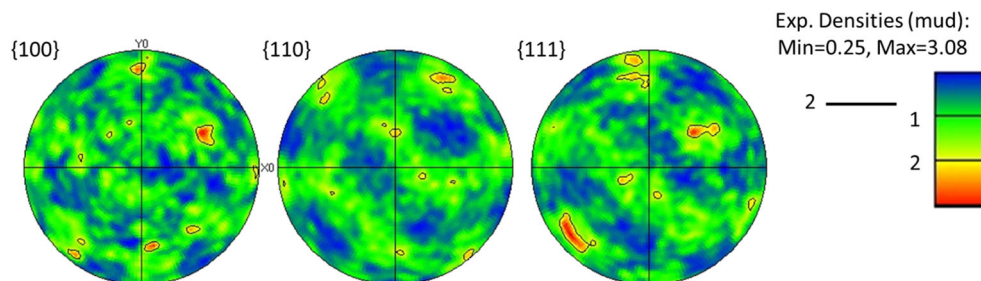
microhardness values have a minor deviation (± 7 HV) from the average microhardness value (160 HV), attributed to the presence of various micro-constituents with different volume fractions within the melt-pool boundaries, the center of the melt pool, versus the HAZ, as described in the microstructure characterization section. Vickers microindentation on different microstructures (Fig. 6b) confirmed that the highest value of microhardness (∼ 175 ± 2 HV) corresponded to the acicular ferrite and bainite (AF + B) regions at the melt-pool boundaries and the lowest value (∼ 150 ± 1 HV) belonged to the coarse polygonal ferrite plus pearlite region in the heat-affected zone $(F+P)_{HAZ}$. It should also be noted that the dominant microstructure of the sample, including the fine ferrite grains with the pearlite lamellae (F + P) formed at the ferrite boundaries, showed the average microhardness of 160 ± 2 HV.

The standard stress versus strain diagrams measured from the WAAM-ER70S-6 samples along both the deposition (horizontal) direction and the building (vertical) direction at room temperature are shown in Fig. 7. Also, the bar chart enclosed in Fig. 7 sum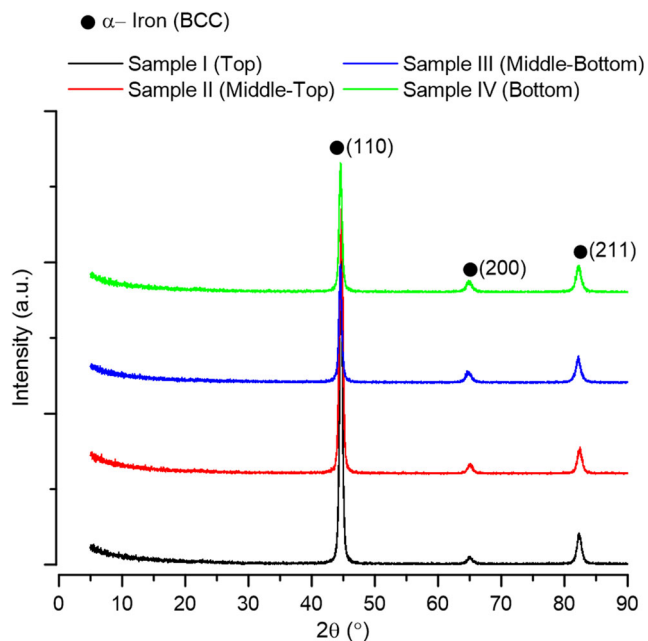marizes the extracted tensile properties, including the yield strength (YS) and ultimate tensile strength (UTS) of the WAAM-ER70S-6 wall along both the deposition and building directions. The average values of UTS and YS of the horizontal and vertical samples confirmed that the additively manufactured wall had approximately similar yield strength and ultimate tensile strength values in both directions (396 ± 26 MPa and 503 ± 21 MPa, respectively), indicating isotropic tensile properties. Analogously, a few recent studies have also reported isotropic tensile strengths for the WAAM-fabricated ferrous parts [20, 29, 46]. However, as clearly visible in Fig. 7, the vertical specimens show a significantly lower elongation than that of the horizontal samples (12 ± 3% and 35 ± 2%, respectively), confirming the prominence of anisotropy in ductility. Such mechanical anisotropy in ductility and toughness commonly occurs in additively manufactured parts and has been reported in many studies for various metals and alloys [47–49].

The consistency in the tensile strength of the vertical and horizontal samples is mostly attributed to the uniformity and homogeneity of the microstructure, as confirmed by the evenly distributed microhardness values in all deposited layers from the bottom to the top of the WAAM-manufactured wall. On the other hand, the drastic reduction in the ductility value from the horizontal sample to the vertical one can plausibly be rationalized by either (i) the presence of manufacturing discontinuities and defects, such as lack of fusion or porosity accumulated in the interlayer regions, (ii) the grain coarsening along the HAZ, and/or (iii) the formation of brittle martensite–austenite (MA) constituent within the bainite lamellar structures. Such a constituent with a brittle nature could potentially fracture during tensile loading of the sample prior to other constituents (F or B), leading to the onset and propagation of internal micro-cracks in early stages of the loading and ultimately failure at significantly lower strain values. Further elucidation of these phenomena is discussed in the following sections.

Figure 8 shows the fractured samples after conducting uniaxial tensile testing herein. Collectively, all vertical tensile samples (Fig. 8a) revealed the development of some transverse cracks, perpendicular to the building direction (or loading direction), formed equidistant from each other during the tensile test. Ultimately, one of those cracks propagated more than the others and resulted in the failure of the sample.
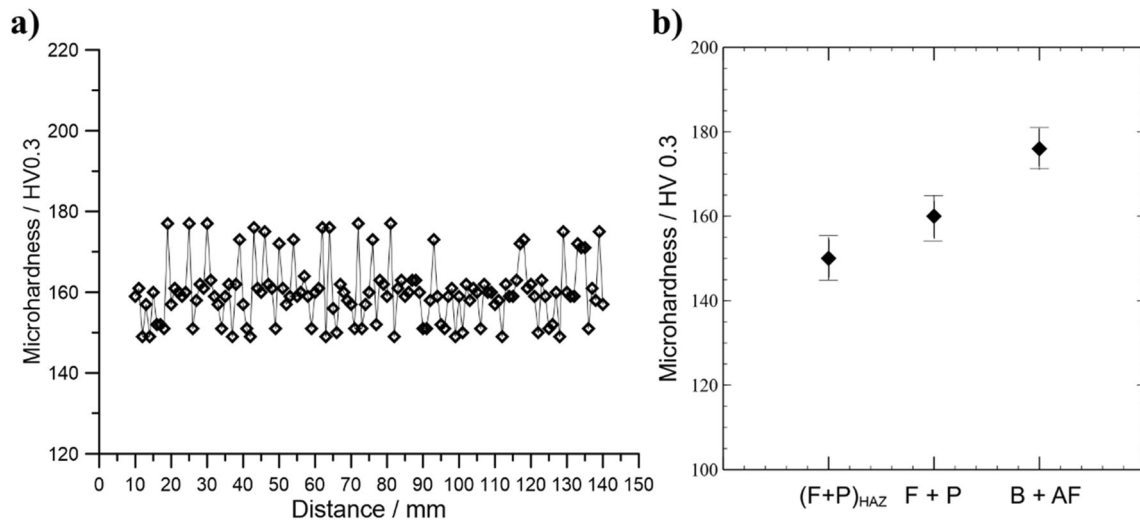

Fig. 5 XRD pattern of the WAAM-ER70S-6 samples taken from different locations along the building direction

Fig. 6 Vickers microhardness distribution on **a** different points on the surface along the building (vertical) direction from the bottom to the top of the wall. **b** The measured microhardness values of different existing constituents in the structure

Formation of similar cracks with constant intervals justifies the supposition that their formation is dictated by the same reason(s). As displayed clearly in Fig. 8b, the onset and propagation of the cracks were detected mainly in the HAZ, which was characterized by grain coarsening due to the high temperature that the material experiences in this region during the solidification of the adjacent bead. The presence of coarse grains in the HAZ deteriorates the mechanical properties, especially the ductility herein, implying that the grain coarsening around HAZ could be one of the main weakening mechanisms in the WAAM-ER70S-6 alloy along the building direction. Therefore, the cracks could potentially nucleate and

propagate preferentially along the heat-affected zones leading to a premature failure through the HAZ.

The impact of the grain size on the strength of the material can be described mathematically using the well-known Hall-Petch equation shown below,

$$\sigma_y = \sigma_0 + Kd^{-1/2} \tag{1}$$

where σ_y is the yield strength of the material, d is the average grain diameter, and σ_0 and K are the material constants, representing the lattice resistance to the dislocation motion and strengthening coefficient, respectively [50]. Therefore, the HAZ can potentially yield prior to the rest of the structure during the tensile loading test. On the contrary, the horizontal samples (Fig. 8a), which were machined primarily from the bulk of each weld bead along the deposition direction, contained the lowest possible HAZ structure incorporated in their gauge length. These samples did not reveal formation of multiple equidistant cracks on their gauge length during tensile testing. Such behavior could be ascribed to the grain size uniformity in this direction.

It should also be noted that fusion boundaries are commonly prone to interpass defects, such as lack of fusion, entrapped gas, and porosity [51, 52]. Although these defects were not detected visually on the as-printed tensile samples or on the polished samples, their existence in the structure is still plausible. Such defects can readily facilitate the brittle fracture by providing potential sites for crack initiation and growth since they can act as strong stress concentrators during tensile loading [53]. Among such defects, the lack of fusion is of particular interest and highly probable to form during multi-pass deposition-based processes, such as WAAM, resulting from the special heat transfer condition between the layers in the sample along the building direction [20]. It is reported that the
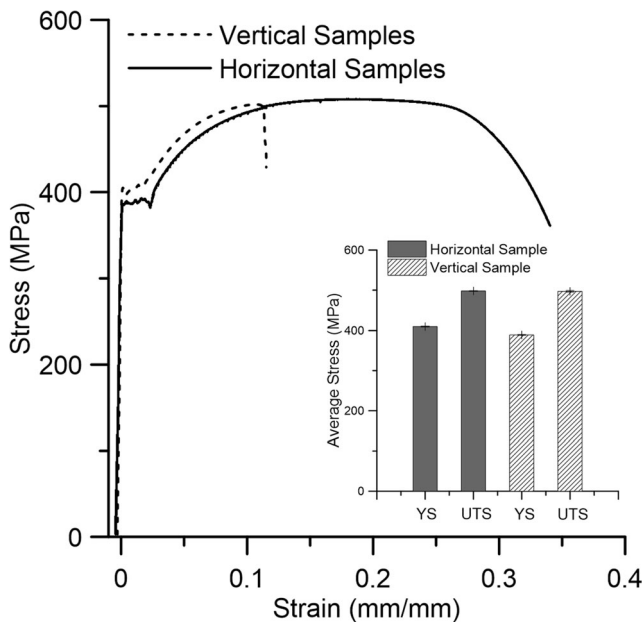

Fig. 7 The stress-strain curves and their corresponding tensile properties for the vertical and horizontal samples
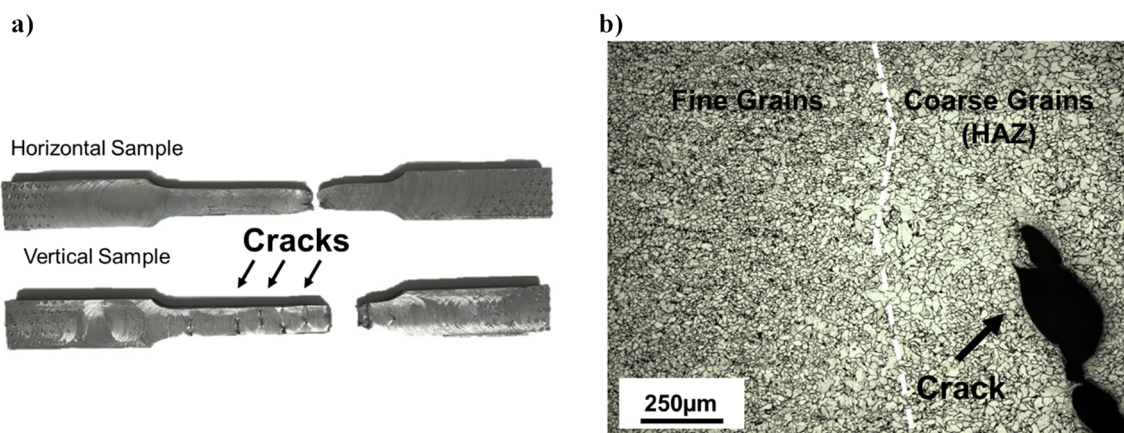
Fig. 8 **a** Tensile samples after fracture. **b** An optical micrograph taken from the cross section of one of the equidistant cracks (shown by the arrows in **a**) formed during tensile testing on the vertical sample

high-heat removal capacity from the interpass regions between the layers can potentially be attributed to a greater portion of the lack of fusion regions within the adjacent beads [20]. The formation of interpass defects can further be investigated by performing non-destructive testing (NDT) methods capable of detecting defects that are not open to the surface, i.e., radiography or ultrasonic testing, which is the subject of a future study.

Another scenario can be defined that could further contribute to the observed lower mechanical integrity of the WAAM sample along the building direction. It is well established that in multi-pass welding of steels, due to increasing the temperature of the interpass regions into the ferrite + austenite phase stability zone between Ac_1 and Ac_3 temperatures, a region so-called the inter-critical heat-affected zone (ICHAZ) adjacent to each melt pool in the previously deposited pass forms [54, 55]. In this region, the austenite phase could potentially nucleate along the bainite lath boundaries or prior austenite grain boundaries. By further diffusion of carbon atoms from the matrix (F + B) into the nucleated austenite phase due to significantly high solid solubility of carbon in austenite phase, the austenite phase can slightly grow, even though the carbon concentration of the ER70S-6 feedstock wire is low. Upon fast cooling of this region, if the carbon content is low, or there are no sufficient austenite stabilizing alloying elements to stabilize the austenite at room temperature (the case of ER70S-6), the reverted austenite phase transforms to the martensite–austenite (MA) constituent, forming localized brittle zones (LBZs) in the ICHAZ [56]. Consequently, these LBZs potentially degrade the toughness of the low-alloy steels by cracking of MA constituent and its detachment from the matrix [18]. As shown in Fig. 9, a closer look at the HAZ of the WAAM-ER70S-6 sample revealed the formation of some of those LBZs. As Fig. 9 reveals, the new MA constituent is nucleated within the bainite lamellar structure. Although the amount of this phase was very minor as compared with the other constituents in the microstructure, it is known that the

formation of martensite–austenite promotes the crack nucleation under tensile loading due to the brittle nature of this phase [57], the induced residual tensile stress on the matrix resulted from the martensitic transformation [57], the incoherency of the MA-ferrite interface that leads to the MA-ferrite interfacial cracking [58], and finally the slip localization in the ferritic matrix around the hard MA phase that could potentially lead to the localized cleavage of the matrix [20]. Therefore, the formation of the MA constituent in the ICHAZ can further contribute to the de-bonding and fracture concentration between the consecutive layers.

Due to the geometry of the vertical samples relative to the building direction, these samples accommodate a high density of melt-pool boundaries and ICHAZs. Therefore, the content of MA phase formed in these samples is significantly higher than that in the horizontal samples. Such microstructural variation between the vertical and horizontal samples can be partially responsible for not only the measured lower ductility of the vertical samples than that of the horizontal samples, but also the formation of the equidistance macro-cracks on the vertical samples during the tensile testing.

To further study the fracture behavior of the samples, the representative SEM fractographs of the horizontal and vertical samples were also analyzed and are depicted in Fig. 10. The fracture surface of the horizontal sample was predominantly comprised of large and deep cup-like depressions and conical dimples with relatively uniform size, indicating occurrence of an extensive plastic deformation and ductile behavior during tensile testing [59]. It confirmed that the fracture is dominated and controlled by microvoids nucleation at regions of localized strain discontinuity, followed by the coalescence of microvoids, leading to a cup and cone-shaped failure surface with the shear lip of around 45° [60].

A different fracture surface for the vertical sample is clearly distinguishable from the micrographs shown in Fig. 10 c and d. It was revealed that the degree of plastic deformation for the vertical sample was not as severe as that in the horizontal
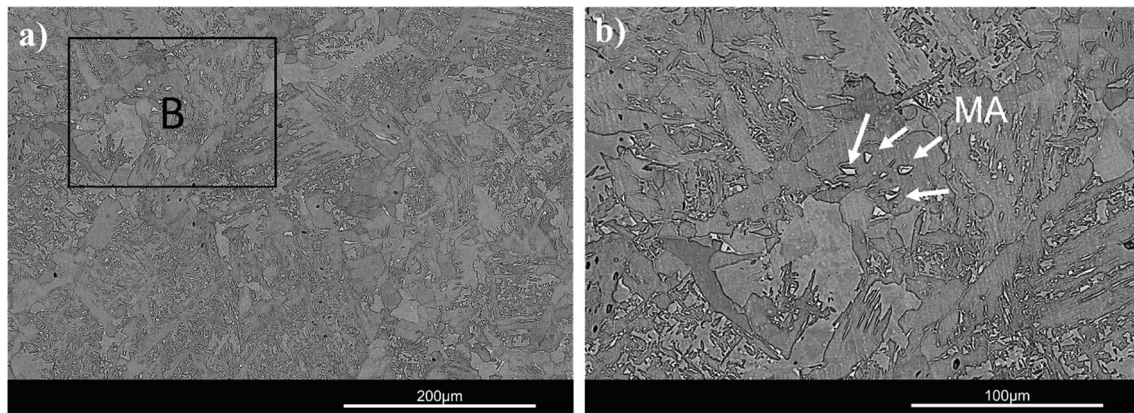
Fig. 9 SEM micrograph taken from **a** the HAZ of the as-printed WAAM-ER70S-6. **b** The higher magnification of the enclosed area in **a** shown by B, demonstrating the formation of MA phase between coarse bainite lamellas

sample. Although dimples can be observed on the fractured surfaces of both vertical and horizontal samples, the morphology of the dimples was found to be different, corresponding to the variation of mechanical behavior and fracture mechanism of the samples during tensile testing [59]. A comparison between dimples formed on the fracture surface of the vertical and horizontal tensile samples at higher magnification (Fig. 10b, d) reveals that their size is smaller and shallower

in the vertical sample, implying that a lower plastic strain was retained by the sample prior to its failure [61, 62]. Moreover, there are some nearly flat areas, including micro-cracks (marked by white arrows in Fig. 10c), in the vertical samples, a compelling evidence for the occurrence of a relatively fast cleavage fracture due to the crack propagation [60]. Therefore, the observed morphological features of the fractured surfaces of both horizontal and vertical samples were found to be in

Fig. 10 SEM micrographs taken from the fractured surfaces after uniaxial tensile testing. **a** and **b** the horizontal sample. **c** and **d** the vertical sample. The side view image from the gauge of the fractured **e** vertical sample and **f** horizontal sample
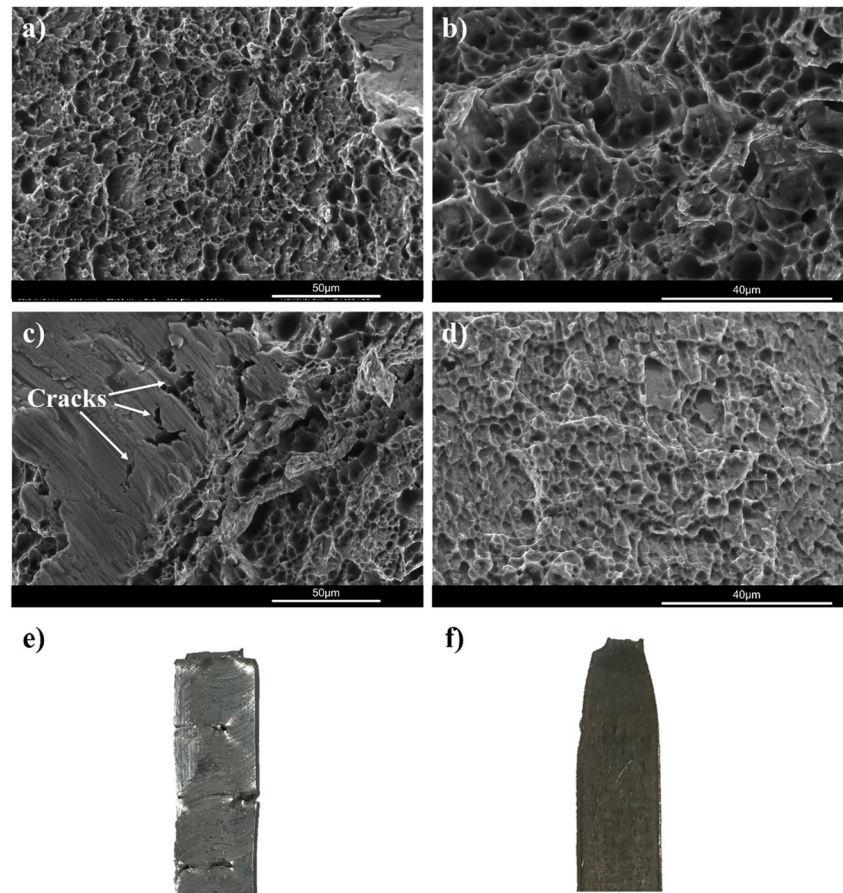
good agreement with their tensile test results, confirming a lower ductility for the vertical samples than the horizontal ones, albeit the tensile strength remained approximately constant.

Likewise, the side view of the fractured samples after uniaxial tensile testing (Fig. 10e, f) confirmed that there is no sign of extensive plastic deformation and necking in vertical samples. On the other hand, an almost homogenous deformation has occurred in the necking area of the horizontal sample, consistent with the results of tensile testing. Hence, it can be concluded that the horizontal samples showed a ductile failure during tensile testing, while vertical samples exhibited a mix ductile-brittle fracture. Due to the similarity of the WAAM process to the conventional welding processes, such as GMAW or GTAW, it was expected that the fabricated wall using WAAM might provoke anisotropy in tensile properties. Depending on the sources of non-uniformity herein, i.e., HAZ grain coarsening, interpass discontinuities, or formation of LBZs, authors may need to come up with various innovative strategies to suppress the measured anisotropy in mechanical properties through optimizing the process parameters, deposition strategy, and/or conducting post-printing heat treatment, which all are subjected to future studies.

4 Conclusions

In this study, ER70S-6 low-carbon low-alloy steel walls were additively manufactured utilizing WAAM technique. Microstructure and mechanical properties of the manufactured component were characterized in different zones and directions. The following conclusions can be drawn:

1. The microstructure of the fabricated wall included two distinct regions across the melt pools, i.e., a wide region composed of fine polygonal ferrite and lamellar pearlite phases as the predominant microstructure of each melt pool, and a confined region at the melt-pool boundaries containing acicular ferrite along with bainite constituents. Formation of different regions with disparate microstructure in the fabricated part is primarily due to the existence of different temperature gradients and solidification rates from the center of each melt pool towards the boundaries of its adjacent solidified tracks.
2. The printed microstructure was primarily comprised of randomly oriented equiaxed grains possessing a weak cubic texture.
3. The specific fabrication methodology in this study, utilizing advanced STT mode for the material's deposition and the adopted y-scanning strategy with alternating directions and 3 mm overlap along the x-axis between the successive passes, along with the implemented cooling intervals between the consecutive layers, contributed to the formation of a similar microstructure in all layers of the wall along the vertical direction. This further contributed to the consistency of the localized mechanical properties along the building direction.
4. The average microhardness of the WAAM-fabricated component was 160 ± 7 HV, which was roughly consistent along the building direction of the component. However, the Vickers microindentation revealed that at the fusion boundaries, where some fraction of acicular ferrite and bainite micro-constituents were detected, the highest microhardness value was reached ($\sim 175 \pm 2$ HV), whereas the heat-affected zone containing coarse ferrite grains revealed the lowest microhardness ($\sim 150 \pm 1$ HV).
5. According to the tensile testing results, comparable yield and ultimate tensile strengths were obtained along the building (vertical) direction and deposition (horizontal) direction of the fabricated WAAM-ER70S-6 part. However, the ductility along the horizontal direction was approximately three times higher than that of the vertical direction. The significantly lower ductility in the building direction was primarily ascribed to the higher density of the interpass regions and the melt-pool boundaries in the vertical direction, where a coarse grain structure in the HAZ, formation of localized brittle zones (MA constituent), and plausibly a higher density of interpass discontinuities exist.
6. The fracture surfaces of both vertical and horizontal samples showed a dimple structure characteristic of microvoid coalescence. However, dimples were found to be larger and deeper on the fracture surface of the horizontal samples, confirming the substantial plastic deformation of the part along the deposition direction as compared with the building direction.

References

1. Liberini M, Astarita A, Campatelli G et al (2017) Selection of optimal process parameters for wire arc additive manufacturing. Procedia CIRP 62:470–474. https://doi.org/10.1016/j.procir.2016.06.124
2. Xiong J, Zhang G (2014) Adaptive control of deposited height in GMAW-based layer additive manufacturing. J Mater Process Technol 214:962–968 https://doi.org/10.1016/j.jmatprotec.2013.11.014
3. Bekker ACM, Verlinden JC (2018) Life cycle assessment of wire + arc additive manufacturing compared to green sand casting and CNC milling in stainless steel DC Power Electrode wire Nozzle Shielding gas Arc Weld pool Workpiece Substrate. J Clean Prod 177:438–447. https://doi.org/10.1016/j.jclepro.2017.12.148
4. Ding D, Pan Z, Cuiuri D, Li H (2015) A multi-bead overlapping model for robotic wire and arc additive manufacturing (WAAM).

Robot Comput Integr Manuf 31:101–110. https://doi.org/10.1016/j.rcim.2014.08.008

5. Shen C, Pan Z, Cuiuri D et al (2016) In-depth study of the mechanical properties for Fe3Al based iron aluminide fabricated using the wire-arc additive manufacturing process. Mater Sci Eng A 669: 118–126. https://doi.org/10.1016/j.msea.2016.05.047

6. FrazierWE (2014)Metal additive manufacturing: a review. JMater Eng Perform 23:1917–1928. https://doi.org/10.1007/s11665-014-0958-z

7. Das S, Bourell DL, Babu SS (2016) Metallic materials for 3D printing. MRS Bull 41:729–741

8. Xiong J, Yin Z, Zhang W (2016) Closed-loop control of variable layer width for thin-walled parts in wire and arc additive manufacturing. J Mater Process Technol 233:100–106. https://doi.org/10.1016/j.jmatprotec.2016.02.021

9. Xiong J, Lei Y, Chen H, Zhang G (2017) Fabrication of inclined thin-walled parts in multi-layer single-pass GMAW-based additive manufacturing with flat position deposition. J Mater Process Technol 240:397–403. https://doi.org/10.1016/j.jmatprotec.2016.10.019

10. Shamsaei N, Yadollahi A, Bian L, Thompson SM (2015) An overview of Direct Laser Deposition for additive manufacturing; part II: mechanical behavior, process parameter optimization and control. Addit Manuf 8:12–35. https://doi.org/10.1016/j.addma.2015.07.002

11. Li Y, Sun Y, Han Q et al (2018) Enhanced beads overlapping model for wire and arc additive manufacturing of multi-layer multi-bead metallic parts. J Mater Process Technol 252:838–848. https://doi.org/10.1016/j.jmatprotec.2017.10.017

12. Chen X, Li J, Cheng X et al (2017) Microstructure and mechanical properties of the austenitic stainless steel 316L fabricated by gas metal arc additive manufacturing. Mater Sci Eng A 703:567–577. https://doi.org/10.1016/j.msea.2017.05.024

13. Xiong J, Li Y, Li R, Yin Z (2018) Influences of process parameters on surface roughness of multi-layer single- pass thin-walled parts in GMAW-based additive manufacturing. J Mater Process Tech 252: 128–136. https://doi.org/10.1016/j.jmatprotec.2017.09.020

14. Yang D, He C, Zhang G (2016) Forming characteristics of thin-wall steel parts by double electrode GMAW based additive manufacturing. J Mater Process Technol 227:153–160. https://doi.org/10.1016/j.jmatprotec.2015.08.021

15. Mohandas T, Reddy GM, Kumar BS (1999) Heat-affected zone softening in high-strength low-alloy steels. J Mater Process Technol 88:284–294

16. Zhang C, Song X, Lu P, Hu X (2012) Effect of microstructure on mechanical properties in weld-repaired high strength low alloy steel. Mater Des 36:233–242. https://doi.org/10.1016/j.matdes.2011.11.016

17. Joshi JR, Potta M, Adepu K et al (2017) Influence of welding techniques on heat affected zone softening of dissimilar metal maraging steel and high strength low alloy steel gas tungsten arc weldments. Trans Indian Inst Met 70:69–81

18. Li X, Ma X, Subramanian SV et al (2014) Influence of prior austenite grain size on martensite–austenite constituent and toughness in the heat affected zone of 700MPa high strength linepipe steel. Mater Sci Eng A 616:141–147. https://doi.org/10.1016/j.msea.2014.07.100

19. Davis CL, King JE (1994) Cleavage initiation in the intercritically reheated coarse-grained heat-affected zone: Part I. Fractographic evidence. Metall Mater Trans A 25:563–573. https://doi.org/10.1007/BF02651598

20. Sridharan N, Noakes MW, Nycz A et al (2018) On the toughness scatter in low alloy C-Mn steel samples fabricated using wire arc additive manufacturing. Mater Sci Eng A 713:18–27. https://doi.org/10.1016/j.msea.2017.11.101

21. Ou W, Mukherjee T, Knapp GL et al (2018) Fusion zone geometries, cooling rates and solidification parameters during wire arc additive manufacturing. Int J Heat Mass Transf 127:1084–1094. https://doi.org/10.1016/j.ijheatmasstransfer.2018.08.111

22. Wilson-Heid AE, Wang Z, McCornac B, Beese AM (2017) Quantitative relationship between anisotropic strain to failure and grain morphology in additively manufactured Ti-6Al-4V. Mater Sci Eng A 706:287–294 https://doi.org/10.1016/j.msea.2017.09.017

23. Yang D, Wang G, Zhang G (2017) Thermal analysis for single-pass multi-layer GMAW based additive manufacturing using infrared thermography. J Mater Process Technol 244:215–224 https://doi.org/10.1016/j.jmatprotec.2017.01.024

24. Farshidianfar MH, Khajepour A, Gerlich A (2016) Real-time control of microstructure in laser additive manufacturing. 1173–1186. https://doi.org/10.1007/s00170-015-7423-5

25. Wang T, Zhang Y, Wu Z, Shi C (2018) Microstructure and properties of die steel fabricated by WAAM using H13 wire. Vaccum 149: 185–189 https://doi.org/10.1016/j.vacuum.2017.12.034

26. Prado-Cerqueira JL, Camacho AM, Diéguez JL et al (2018) Analysis of favorable process conditions for the manufacturing of thin-wall pieces of mild steel obtained by wire and arc additive manufacturing (WAAM). Mater (Basel, Switzerland) 11:1449 https://doi.org/10.3390/ma11081449

27. Wang Z, Palmer TA, Beese AM (2016) Effect of processing parameters on microstructure and tensile properties of austenitic stainless steel 304L made by directed energy deposition additive manufacturing. Acta Mater 110:226–235 https://doi.org/10.1016/j.actamat.2016.03.019

28. Wang F, Williams S, Colegrove P, Antonysamy AA Microstructure and mechanical properties of wire and arc additive manufactured Ti-6Al-4V. https://doi.org/10.1007/s11661-012-1444-6

29. Haden CV, Zeng G, Carter FM et al (2017) Wire and arc additive manufactured steel: tensile and wear properties. Addit Manuf 16: 115–123. https://doi.org/10.1016/j.addma.2017.05.010

30. Fachinotti VD, Cardona A, Baufeld B, Van der Biest O (2012) Finite-element modelling of heat transfer in shaped metal deposition and experimental validation. Acta Mater 60:6621–6630. https://doi.org/10.1016/j.actamat.2012.08.031

31. Hu R, Chen X, Yang G et al (2018) Metal transfer in wire feeding-based electron beam 3D printing: modes, dynamics, and transition criterion. Int J Heat Mass Transf 126:877–887. https://doi.org/10.1016/j.ijheatmasstransfer.2018.06.033

32. Gook S, Gumenyuk A, Rethmeier M (2014) Hybrid laser arc welding of X80 and X120 steel grade. Sci Technol Weld Join 19: 15–24

33. Alagesan R, Kumar TS (2014) Optimization of welding cycle time by establishing full GMAW process (STT and P-GMAW) through a newly designed semi-automatic welding positioner. Int J Res Eng Technol 3

34. DeRuntz BD (2003) Assessing the benefits of surface tension transfer welding to industry. J Ind Technol 19:55–62

35. Stava EK (1993) The surface tension transfer power source, a new, low-spatter arc welding machine. Weldit-Journal 1:25–29

36. American Welding Society (2005) Specification for carbon steel electrodes and rods for gas shielded arc welding. Am Weld Soc 2005:44 https://doi.org/978-0-87171-530-2

37. 28M AWSA 28/A5 (2005) Specification for low alloy steel electrodes and rods for gas shielded arc welding

38. ASTM Int (2015) Standard test methods for tension testing of metallic materials 1. Astm i, pp 1–27 https://doi.org/10.1520/E0008

39. Colegrove PA, Coules HE, Fairman J et al (2013) Microstructure and residual stress improvement in wire and arc additively manufactured parts through high-pressure rolling. J Mater Process Technol 213:1782–1791 https://doi.org/10.1016/j.jmatprotec.2013.04.012

40. Haselhuhn AS, Wijnen B, Anzalone GC et al (2015) In situ formation of substrate release mechanisms for gas metal arc weld metal 3-D printing. J Mater Process Technol 226:50–59 https://doi.org/10.1016/j.jmatprotec.2015.06.038

41. Godefroid LB, Cândido LC, Toffolo RVB, Barbosa LHS (2014) Microstructure and mechanical properties of two API steels for iron ore pipelines. Mater Res 17:114–120 https://doi.org/10.1590/S1516-14392014005000068

42. Tweed JH, Knott JF (1983) Effect of reheating on microstructure and toughness of C–Mn weld metal. Met Sci 17:45–54 https://doi.org/10.1179/030634583790427603

43. Zhang C, Li Y, Gao M, Zeng X (2018) Wire arc additive manufacturing of Al-6Mg alloy using variable polarity cold metal transfer arc as power source. Mater Sci Eng A 711:415–423 https://doi.org/10.1016/j.msea.2017.11.084

44. Yang KV, Shi Y, Palm F et al (2018) Columnar to equiaxed transition in Al-Mg(-Sc)-Zr alloys produced by selective laser melting. Scr Mater 145:113–117 https://doi.org/10.1016/j.scriptamat.2017.10.021

45. Biscuola VB, Martorano MA (2008) Mechanical blocking mechanism for the columnar to equiaxed transition. Metall Mater Trans A 39:2885–2895 https://doi.org/10.1007/s11661-008-9643-x

46. Suryakumar S, Karunakaran KP, Chandrasekhar U, Somashekara MA (2013) A study of the mechanical properties of objects built through weld-deposition. Proc Inst Mech Eng Part B J Eng Manuf 227:1138–1147 https://doi.org/10.1177/0954405413482122

47. Carroll BE, Palmer TA, Beese AM (2015) Anisotropic tensile behavior of Ti-6Al-4V components fabricated with directed energy deposition additive manufacturing. Acta Mater 87:309–320 https://doi.org/10.1016/j.actamat.2014.12.054

48. Thijs L, Sistiaga MLM, Wauthle R et al (2013) Strong morphological and crystallographic texture and resulting yield strength anisotropy in selective laser melted tantalum. Acta Mater 61:4657–4668

49. Zhang Q, Chen J, Zhao Z et al (2016) Microstructure and anisotropic tensile behavior of laser additive manufactured TC21 titanium alloy. Mater Sci Eng A 673:204–212 https://doi.org/10.1016/j.msea.2016.07.040

50. Hall EO (1951) The deformation and ageing of mild steel: III discussion of results. Proc Phys Soc Sect B 64:747–753 https://doi.org/10.1088/0370-1301/64/9/303

51. Lopez A, Bacelar R, Pires I et al (2018) Non-destructive testing application of radiography and ultrasound for wire and arc additive manufacturing. Addit Manuf 21:298–306. https://doi.org/10.1016/j.addma.2018.03.020

52. Szost BA, Terzi S, Martina F et al (2016) A comparative study of additive manufacturing techniques: residual stress and microstructural analysis of CLAD and WAAM printed Ti-6Al-4V components. Mater Des 89:559–567 https://doi.org/10.1016/j.matdes.2015.09.115

53. Kudzal A, McWilliams B, Hofmeister C et al (2017) Effect of scan pattern on the microstructure and mechanical properties of powder bed fusion additive manufactured 17-4 stainless steel. Mater Des 133:205–215 https://doi.org/10.1016/j.matdes.2017.07.047

54. Kim BC, Lee S, Kim NJ, Lee DY (1991) Microstructure and local brittle zone phenomena in high-strength low-alloy steel welds. Metall Trans A 22:139–149 https://doi.org/10.1007/BF03350956

55. Akselsen OM, Grong Ø, Solberg JK (1987) Structure–property relationships in intercritical heat affected zone of low-carbon microalloyed steels. Mater Sci Technol 3:649–655 https://doi.org/10.1179/mst.1987.3.8.649

56. Li Y, Baker TN (2010) Effect of morphology of martensite–austenite phase on fracture of weld heat affected zone in vanadium and niobium microalloyed steels. Mater Sci Technol 26:1029–1040 https://doi.org/10.1179/026708309X12512744154360

57. Lambert A, Lambert A, Drillet J et al (2000) Microstructure of martensite–austenite constituents in heat affected zones of high strength low alloy steel welds in relation to toughness properties. Sci Technol Weld Join 5:168–173 https://doi.org/10.1179/136217100101538164

58. Huda N, Midawi ARH, Gianetto J et al (2016) Influence of martensite-austenite (MA) on impact toughness of X80 line pipe steels. Mater Sci Eng A 662:481–491. https://doi.org/10.1016/j.msea.2016.03.095

59. Shi X, Ma S, Liu C et al (2017) Selective laser melting-wire arc additive manufacturing hybrid fabrication of Ti-6Al-4V alloy: Microstructure and mechanical properties. Mater Sci Eng A 684:196–204 https://doi.org/10.1016/j.msea.2016.12.065

60. Xu X, Ganguly S, Ding J et al (2017) Microstructural evolution and mechanical properties of maraging steel produced by wire+arc additive manufacture process. Mater Charact

61. Murr LE, Quinones SA, Gaytan SM et al (2009) Microstructure and mechanical behavior of Ti–6Al–4V produced by rapid-layer manufacturing, for biomedical applications. J Mech Behav Biomed Mater 2:20–32 https://doi.org/10.1016/j.jmbbm.2008.05.004

62. Murr LE, Esquivel EV, Quinones SA et al (2009) Microstructures and mechanical properties of electron beam-rapid manufactured Ti–6Al–4V biomedical prototypes compared to wrought Ti–6Al–4V. Mater Charact 60:96–105 https://doi.org/10.1016/j.matchar.2008.07.006